

EUROPEAN ORGANIZATION FOR NUCLEAR RESEARCH
Laboratory for Particle Physics

Departmental Report

CERN/AT 2007-33 (MCS)

**ANALYTIC MODELS FOR THE CALCULATION
OF THE IRON YOKE CONTRIBUTION
IN SUPERCONDUCTING ACCELERATOR MAGNETS**

N. Schwerg, C. Vollinger

The superconducting coil of an accelerator magnet is usually surrounded by magnetic material, the iron yoke, in order to enhance the field in the aperture and to reduce the fringe field outside the magnet.

For the calculation of the magnetic field of such superconducting magnets, numerical methods, typically FEM are used. Nevertheless, analytic solutions of simplified geometries are still needed in order to cross-check numerically obtained results and gain deeper understanding of the underlying principles.

For the calculation of the effect of the iron yoke on the field distribution and field quality of superconducting coils as a first approximation a circular hollow cylinder of high permeable material could be used.

CERN, Accelerator Technology Department, Geneva, Switzerland

1 Introduction

The superconducting coil of an accelerator magnet is usually surrounded by magnetic material, the iron yoke, in order to enhance the field in the aperture and to reduce the fringe field outside the magnet.

For the calculation of the magnetic field of such superconducting magnets, typically FEM methods are used. For our calculations, we used the coupled method of boundary elements and finite elements which, in addition, allows to omit a meshing of the coil. In this way, the superconducting cables are represented by line currents and the field resulting from any permeable material can be conveniently solved. Nevertheless, analytic solutions of simplified geometries are still needed in order to cross-check numerically obtained results and gain deeper understanding of the underlying principles.

For the calculation of the effect of the iron yoke on the field distribution and field quality of superconducting coils as a first approximation a circular hollow cylinder of high permeable material could be used.

By solving the vector potential of a circular hollow cylinder including three different materials a powerful and general approach is obtained which can be easily adapted and simplified for different problems, *e.g.*, the determination of the influence of the iron yoke thickness on the field quality¹ or the determination of the saturation current.

All derivations and theoretical aspects of the obtained solutions can be found in the appendix.

2 Circular Hollow Cylinder - Three Arbitrary Materials

We consider a problem with three different materials. The geometry consists of a circular hollow cylinder with inner radius a and outer radius b with materials of permeabilities μ_1 , μ_2 and μ_3 as illustrated in fig. 1. Inside the hollow cylinder one line current I is placed at an arbitrary position $x = r_I < a$. The magnetic vector potential for all three domains can be calculated from the potential of a line current by fulfilling the boundary conditions and the general solution of the LAPLACE equation in cylindrical coordinates. Due to the z -directed current, the vector potential has only a z -component. The detailed derivation

¹The field quality is expressed in terms of the so-called multipole field errors following the European definition (see appendix A).

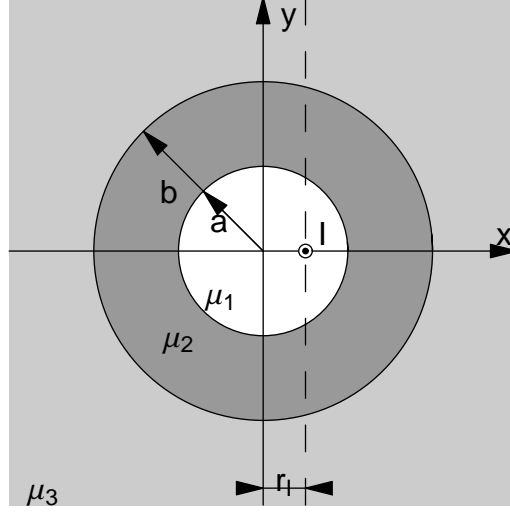


Figure 1: Geometry of a circular hollow cylinder of inner radius a and outer radius b . The tube is filled by a material of permeability μ_2 and surrounded by two materials of different permeabilities (μ_1 inside and μ_3 outside).

is shown in Appendix B and here only the resulting vector potentials are given:

$$\begin{aligned}
A_{1,z}^{\rho < r_I}(\rho, \phi) &= \frac{(\mu_1 - \mu_2)I}{2\pi} \ln\left(\frac{a}{R_0}\right) + \frac{(\mu_2 - \mu_3)I}{2\pi} \ln\left(\frac{b}{R_0}\right) - \frac{\mu_1 I}{2\pi} \ln\left(\frac{r_I}{R_0}\right) \\
&+ \frac{\mu_1 I}{2\pi} \sum_{n=1}^{\infty} \frac{1}{n} \left(\left(\frac{\rho}{r_I}\right)^n - \frac{\alpha_{12} \left(\frac{\rho}{a^2/r_I}\right)^n + \alpha_{23} \left(\frac{\rho}{b^2/r_I}\right)^n}{1 + \alpha_{12}\alpha_{23} \left(\frac{a}{b}\right)^{2n}} \right) \cos(n\phi), \quad (1)
\end{aligned}$$

$$\begin{aligned}
A_{1,z}^{r_I < \rho < a}(\rho, \phi) &= \frac{(\mu_1 - \mu_2)I}{2\pi} \ln\left(\frac{a}{R_0}\right) + \frac{(\mu_2 - \mu_3)I}{2\pi} \ln\left(\frac{b}{R_0}\right) - \frac{\mu_1 I}{2\pi} \ln\left(\frac{\rho}{R_0}\right) \\
&+ \frac{\mu_1 I}{2\pi} \sum_{n=1}^{\infty} \frac{1}{n} \left(\left(\frac{r_I}{\rho}\right)^n - \frac{\alpha_{12} \left(\frac{\rho}{a^2/r_I}\right)^n + \alpha_{23} \left(\frac{\rho}{b^2/r_I}\right)^n}{1 + \alpha_{12}\alpha_{23} \left(\frac{a}{b}\right)^{2n}} \right) \cos(n\phi), \quad (2)
\end{aligned}$$

$$\begin{aligned}
A_{2,z}^{a < \rho < b}(\rho, \phi) &= \frac{(\mu_2 - \mu_3)I}{2\pi} \ln\left(\frac{b}{R_0}\right) - \frac{\mu_2 I}{2\pi} \ln\left(\frac{\rho}{R_0}\right) \\
&+ \frac{\mu_2 I}{2\pi} \sum_{n=1}^{\infty} \frac{1}{n} \frac{-\alpha_{23}\beta_{12} \left(\frac{\rho}{b^2/r_I}\right)^n + \beta_{12} \left(\frac{r_I}{\rho}\right)^n}{1 + \alpha_{12}\alpha_{23} \left(\frac{a}{b}\right)^{2n}} \cos(n\phi) \quad (3)
\end{aligned}$$

$$A_{3,z}^{b < \rho}(\rho, \phi) = -\frac{\mu_3 I}{2\pi} \ln\left(\frac{\rho}{R_0}\right) + \frac{\mu_3 I}{2\pi} \sum_{n=1}^{\infty} \frac{1}{n} \frac{\beta_{12}\beta_{23} \left(\frac{r_I}{\rho}\right)^n}{1 + \alpha_{12}\alpha_{23} \left(\frac{a}{b}\right)^{2n}} \cos(n\phi). \quad (4)$$

Here R_0 denotes an arbitrary reference radius introduced to get a dimensionless argument of the logarithm. It cancels out as soon as two line currents of opposite direction are considered and has no influence on the magnetic field. The coefficients α_{nm} and β_{nm} with $n = 1, 2$ and $m = n + 1$ are defined as

$$\alpha_{nm} = \frac{\mu_n - \mu_m}{\mu_n + \mu_m}, \quad (5)$$

$$\beta_{nm} = \frac{2\mu_n}{\mu_n + \mu_m}. \quad (6)$$

3 Permeable Bore

A common way to approximate the effect of a circular iron yoke of superconducting magnets is to replace the yoke by a permeable area with a bore [1]. This approach is valid for a linear iron material, *i.e.*, for fields smaller than the saturation field strength (see section 3.1), and for a yoke thick enough to close most field lines inside (see also section 4.1).

The result can be derived from the solutions of the general problem² by setting the permeabilities of the areas 2 and 3 to the same value ($\mu_2 = \mu_3$). The simplified geometry is shown in fig. 2.

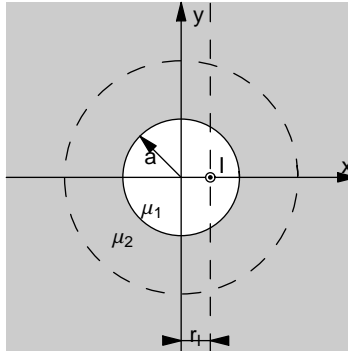


Figure 2: Geometry of a single line current in a bore of permeable material.

The constants α_{nm} and β_{nm} then read:

$$\alpha_{12} = \frac{\mu_1 - \mu_2}{\mu_2 + \mu_1}, \quad \beta_{12} = \frac{2\mu_1}{\mu_2 + \mu_1}, \quad (7)$$

$$\alpha_{23} = 0, \quad \beta_{23} = 1. \quad (8)$$

²For the solution of the general problem of three materials, there are three ways to describe the bore inside the permeable area. It can be either assumed that area 1 and 2 or that area 2 and 3 are of the same material properties. Furthermore the geometry is given for an inner radius a equaling the outer radius b and $\mu_2 \neq \infty$. All three approaches yield the same result and so they are an easy test of correctness of the derived terms.

This significantly simplifies the terms for the vector potential and the solution for area 2 and 3 become identical. The resulting vector potentials read

$$A_{\text{Bore},1,z}^{\rho < r_I}(\rho, \phi) = \frac{(\mu_1 - \mu_2)I}{2\pi} \ln\left(\frac{a}{R_0}\right) - \frac{\mu_1 I}{2\pi} \ln\left(\frac{r_I}{R_0}\right) + \frac{\mu_1 I}{2\pi} \sum_{n=1}^{\infty} \frac{1}{n} \left(\left(\frac{\rho}{r_I}\right)^n - \alpha_{12} \left(\frac{\rho}{a^2/r_I}\right)^n \right) \cos(n\phi), \quad (9)$$

$$A_{\text{Bore},1,z}^{r_I < \rho < a}(\rho, \phi) = \frac{(\mu_1 - \mu_2)I}{2\pi} \ln\left(\frac{a}{R_0}\right) - \frac{\mu_1 I}{2\pi} \ln\left(\frac{\rho}{R_0}\right) + \frac{\mu_1 I}{2\pi} \sum_{n=1}^{\infty} \frac{1}{n} \left(\left(\frac{r_I}{\rho}\right)^n - \alpha_{12} \left(\frac{\rho}{a^2/r_I}\right)^n \right) \cos(n\phi), \quad (10)$$

$$A_{\text{Bore},2,z}^{a < \rho < b}(\rho, \phi) = -\frac{\mu_2 I}{2\pi} \ln\left(\frac{\rho}{R_0}\right) + \beta_{12} \frac{\mu_2 I}{2\pi} \sum_{n=1}^{\infty} \frac{1}{n} \left(\frac{r_I}{\rho}\right)^n \cos(n\phi), \quad (11)$$

$$A_{\text{Bore},3,z}^{b < \rho}(\rho, \phi) = A_{\text{Bore},2,z}. \quad (12)$$

Figure 3 shows the resulting field distribution for different values of μ_2 . From the plots, two observations can be made: 1) With increasing values of the outer permeability, μ_2 , the field density outside the bore increases. Note that this would not be the case if two line currents of opposite signs were considered inside the bore. 2) At the boundary of high permeable domains, field lines are expected to be perpendicular to the surface. This is not the case here! Both effects are studied and explained in Appendix C.

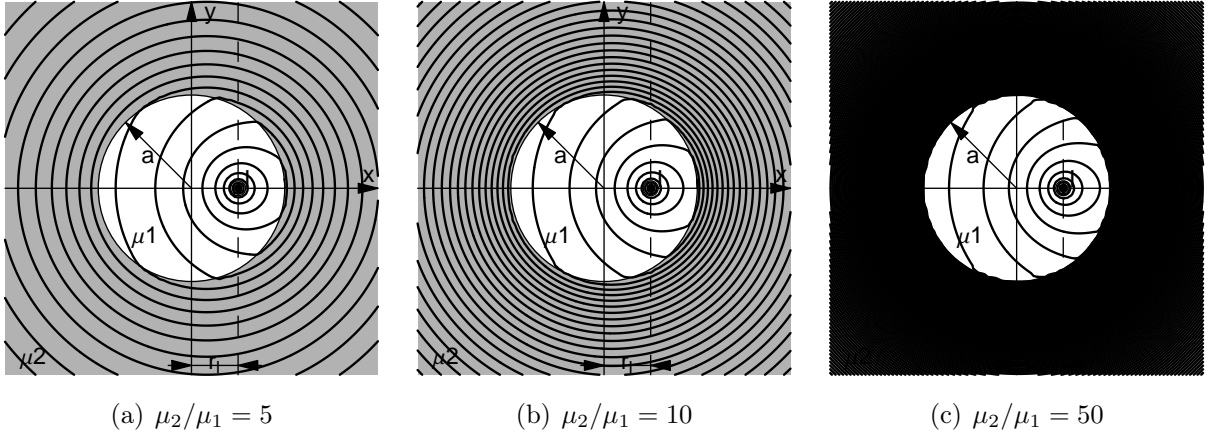


Figure 3: Field distribution of the magnetic induction for a single straight line current inside a bore of permeable material. With increasing value of μ_2 the field density in area 2 increases, too.

3.1 The Saturation Current

When introducing the general solution of the three material problem the assumption of linear and homogeneous materials was made. For realistic materials, as *e.g.*, the magnetic steel of the iron yoke of the LHC or NED dipole, this is only valid as long as the magnetic field stays below the value where the yoke material starts to behave non-linearly and saturates (roughly around 2 T - see fig. 4). The analytical model is limited by the so-called saturation field strength and thus the corresponding saturation current.

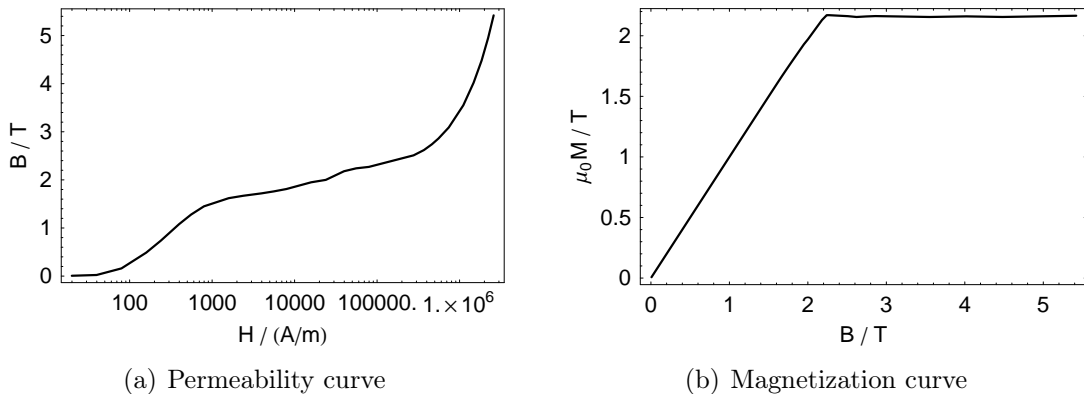


Figure 4: Permeability curve and magnetization-curve as used for the LHC main dipoles and the NED magnet [2]. One can see that the magnetization leaves the linear regime at roughly 2 T and stays more or less constant for higher values.

The saturation current can be obtained by increasing the current of any given geometry until the maximum field inside the material reaches the saturation field. For this purpose, the iron yoke is modeled by means of a bore of radius a in a material of linear and homogeneous permeability μ_{lin} , allowing to derive a closed expression for the saturation current. In order to keep the calculation as general and simple as possible, no specific coil cross section layout is considered, instead two line currents are placed symmetrically at $x = \pm r_P$. The field of the magnetic induction in the permeable material can easily be calculated by means of the imaging method

$$\mathbf{B}_{\text{iron}}(x, y) = \beta_{12} \left(-\mathbf{B}_1(x + r_P, y) + \mathbf{B}_1(x - r_P, y) \right)$$

where \mathbf{B}_1 denotes the field of magnetic induction of a single line current in a material of permeability μ_2 . In this case, β_{12} is given by Eq. (65).

The field maximum is expected in close vicinity to the coil, located on the boundary. By using the FOURIER expansion of the two line currents, the two maxima of the modulus on the boundary can be identified on the x -axis³. Due to the symmetry of the coil the field

³That is different from what one would expect. For dipole coils in magnet construction, the field maximum and the saturation starts at the poles [3].

of magnetic induction on the axis is only $\pm y$ -directed.

$$\begin{aligned}\max_{\rho=a} |\mathbf{B}_{\text{iron}}| &= |B_{\text{iron},y}(x = \pm a, 0)| \\ &= \beta_{12} \frac{\mu_{\text{lin}} I}{\pi} \frac{r_{\text{P}}}{a^2 - r_{\text{P}}^2}\end{aligned}\quad (13)$$

For high values of μ_{lin} the product $\mu_{\text{lin}}\beta_{12}$ can be replaced by μ_0 (for $\mu_{\text{lin}} = 50\mu_0$ the factor gives already $\approx 0.98\mu_0$). Substituting the current I by the ampere turns NI (with N the number of turns and I the current per turn) and setting $B_{\text{sat}} = \max_{\rho=a} |\mathbf{B}_{\text{iron}}|$, the ampere turns are given as:

$$NI = \pi \frac{B_{\text{sat}}}{\mu_0} r_{\text{P}} \left(\left(\frac{a}{r_{\text{P}}} \right)^2 - 1 \right). \quad (14)$$

For an exemplary calculation a coil of 90 conductors and a mean positioning radius of 0.075 m is considered. The relative permeability of the iron yoke is chosen to be 500, the saturation field set to 2 T, and the inner yoke radius to 0.125 m. For this geometry, the term yields a current of 7.4 kA. This result is consistent with the numerically determined saturation current of the NED 88 mm magnet of 7.5 kA[4]. For the LHC main bending magnets the formula gives a saturation current of 11.5 kA which is still in good agreement with the numerically determined saturation current of ≈ 9 kA considering the double aperture yoke.

ANSORGE [5] published a third method to determine the saturation current for an iron yoke of finite thickness. It shall be mentioned here because of its beauty and simplicity: From the total flux of one pole entering the iron tube wall, he determines the minimum thickness of the iron yoke in order to guide the flux without exceeding the saturation field (magnetic induction) assuming a homogenous flux distribution inside the shell. In the same way, it is possible to calculate the maximum energization current for a given wall thickness. For an infinite thick tube this approach means to limit the mean flux density to the saturation flux density and would thus yield greater values than the approaches shown above.

3.2 The Effect on Multipole Errors

In [1, p.144 ff] it is shown that the multipole errors of a single line current can be derived by comparing the expression for the radial field with the general multipole expansion. Furthermore, a geometry of an up-down symmetry only gives normal multipole errors which are at maximum for zero positioning angle of the line current.

In order to reduce the degrees of freedom for this estimation a single line current at an arbitrary position on the x -axis placed in a circular bore of a permeable material is assumed. Only the position of the line current with respect to the bore radius and the material permeability are varied. For a more general result considering the positioning angle as well, the same approach could be used by applying the sine addition theorems (see also B.4).

Deriving the normal magnetic induction from Eq. (9), the normal multipole errors are given as:

$$B_{n,\text{Bore}} = -\frac{\mu_1 I}{2\pi} \frac{r_0^{n-1}}{r_I^n} \left(1 - \alpha_{12} \left(\frac{r_I}{a} \right)^{2n} \right) \quad (15)$$

where r_0 denotes the reference radius. This result can easily be split into the multipole error induced by the line current $B_{n,|}$ and the added $\Delta B_{n,\text{Bore}}$ of the virtual image current. Then the added relative normal multipole error reads

$$\frac{B_{n,\text{Bore}} - B_{n,|}}{B_{n,|}} = \frac{\Delta B_{n,\text{Bore}}}{B_{n,|}} = -\alpha_{12} \left(\frac{r_I}{a} \right)^{2n}. \quad (16)$$

Figure 5 shows the dependence of the added multipole error on the inner bore radius for a material with a permeability going to infinity. The dependence is given as a function of the bore radius a with respect to the positioning radius r_I . The plot shows, *e.g.*, for a bore radius twice the positioning radius of the line current, $a = 2r_I$, all multipoles of order 5 and higher show only a negligible influence of the outer material. For positioning radii that are even smaller with respect to the bore radius, *e.g.*, $a = 5r_I$, only the main field component is influenced by the surrounding permeable material.

4 Permeable tube

The iron yoke of real superconducting magnets is more or less a tube of a high permeable material. This is usually modeled by means of the imaging method or calculated, *e.g.*, with the finite element method. In order to determine the applicability of the imaging method and to give an analytical expression, the solution shall be derived directly from the general solution for circular geometries (section B.4).

For this purpose, the general geometry is simplified by setting the permeabilities of area 1 and 3 identical ($\mu_1 = \mu_3$) and the permeability of area 2 to a higher value ($\mu_2 > \mu_1$). All other quantities remain unchanged. The geometry of the single line current inside the permeable tube is shown in fig. 6.

With the assumptions given above, the constants α_{nm} and β_{nm} read:

$$\alpha_{12} = \frac{\mu_1 - \mu_2}{\mu_2 + \mu_1}, \quad \beta_{12} = 1 + \alpha_{12}, \quad (17)$$

$$\alpha_{23} = -\alpha_{12}, \quad \beta_{23} = 1 - \alpha_{12}. \quad (18)$$

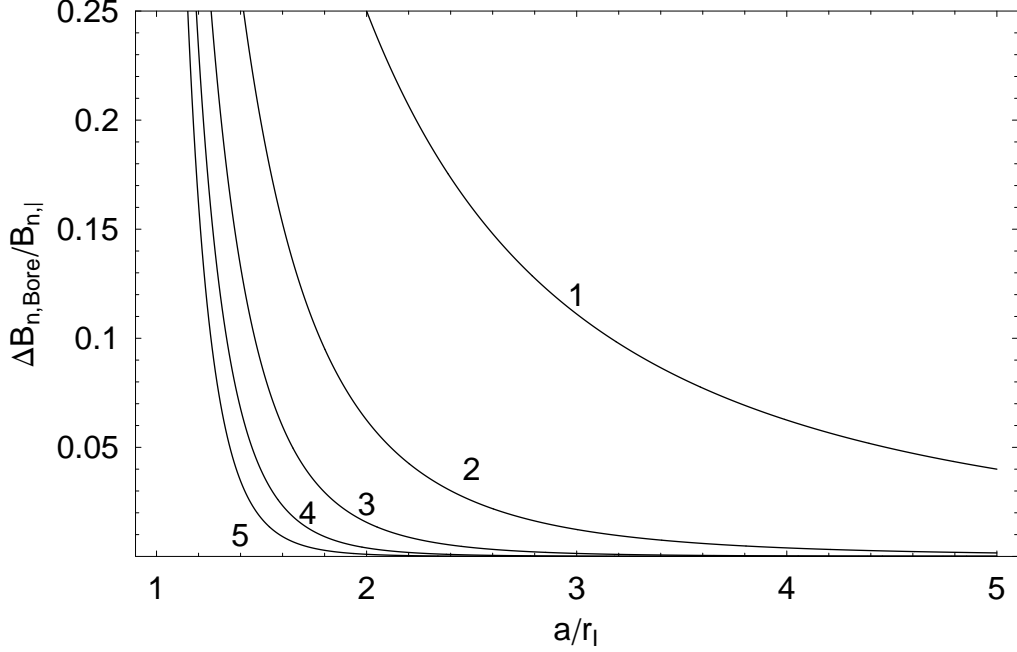


Figure 5: For a line current inside a circular bore within a material with infinite permeability, multipole errors are induced by the line current and its virtual image current replacing the outside material of infinite permeability. The dependence of the the additional multipole errors on the inner bore radius with respect to the positioning radius of the considered strand is shown.

The vector potentials result to:

$$\begin{aligned}
A_{1,z}^{\rho < r_I}(\rho, \phi) &= \frac{(\mu_1 - \mu_2)I}{2\pi} \ln\left(\frac{a}{b}\right) - \frac{\mu_1 I}{2\pi} \ln\left(\frac{r_I}{R_0}\right) \\
&+ \frac{\mu_1 I}{2\pi} \sum_{n=1}^{\infty} \frac{1}{n} \left(\left(\frac{\rho}{r_I}\right)^n - \alpha_{12} \frac{\left(\frac{\rho}{a^2/r_I}\right)^n - \left(\frac{\rho}{b^2/r_I}\right)^n}{1 - \alpha_{12}^2 \left(\frac{a}{b}\right)^{2n}} \right) \cos(n\phi), \quad (19)
\end{aligned}$$

$$\begin{aligned}
A_{1,z}^{r_I < \rho < a}(\rho, \phi) &= \frac{(\mu_1 - \mu_2)I}{2\pi} \ln\left(\frac{a}{b}\right) - \frac{\mu_1 I}{2\pi} \ln\left(\frac{\rho}{R_0}\right) \\
&+ \frac{\mu_1 I}{2\pi} \sum_{n=1}^{\infty} \frac{1}{n} \left(\left(\frac{r_I}{\rho}\right)^n - \alpha_{12} \frac{\left(\frac{\rho}{a^2/r_I}\right)^n - \left(\frac{\rho}{b^2/r_I}\right)^n}{1 - \alpha_{12}^2 \left(\frac{a}{b}\right)^{2n}} \right) \cos(n\phi), \quad (20)
\end{aligned}$$

$$\begin{aligned}
A_{2,z}^{a < \rho < b}(\rho, \phi) &= \frac{(\mu_2 - \mu_3)I}{2\pi} \ln\left(\frac{b}{R_0}\right) - \frac{\mu_2 I}{2\pi} \ln\left(\frac{\rho}{R_0}\right) \\
&+ \frac{\mu_2 I}{2\pi} \sum_{n=1}^{\infty} \frac{1}{n} \beta_{12} \frac{\alpha_{12} \left(\frac{\rho}{b^2/r_I}\right)^n + \left(\frac{r_I}{\rho}\right)^n}{1 - \alpha_{12}^2 \left(\frac{a}{b}\right)^{2n}} \cos(n\phi), \quad (21)
\end{aligned}$$

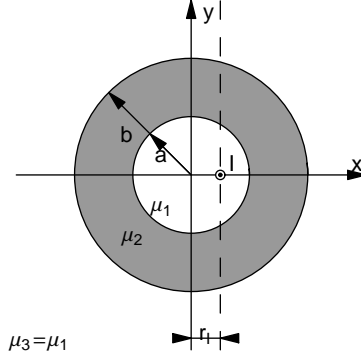


Figure 6: Geometry of a single line current inside the permeable tube.

$$A_{3,z}^{b < \rho}(\rho, \phi) = -\frac{\mu_1 I}{2\pi} \ln\left(\frac{\rho}{R_0}\right) + \frac{\mu_1 I}{2\pi} \sum_{n=1}^{\infty} \frac{1}{n} \frac{\beta_{12}(1 - \alpha_{12}) \left(\frac{r_I}{\rho}\right)^n}{1 - \alpha_{12}^2 \left(\frac{a}{b}\right)^{2n}} \cos(n\phi). \quad (22)$$

As could be expected, the influence of the permeable tube vanishes for $a = b$ with $\mu_2 \neq \infty$ and also for $\mu_2 = \mu_1$. For $b \rightarrow \infty$ the Eqs. (19) to (22) transform to the expressions for the bore in a permeable area given in Eqs. (10) and (12). Furthermore the expressions are in good agreement with the results published in literature as [6].

In fig. 7 the distribution of the magnetic induction is shown for three tubes of different permeabilities. It can be seen that for increasing permeability of the tube more and more magnetic flux is concentrated in the tube walls like for the permeable core of toroidal coils. Mathematically this is related to the same fact as explained for the permeable bore and it also vanishes if the current sum inside the tube is set to zero (see appendix C.1).

Considering Eq. (22) for a tube made of infinitely permeable material, it can be seen that the field of the line current outside the tube is not screened, but the virtual position of the line current is moved to the center of the tube. This is in agreement with $\oint \mathbf{H} \cdot d\mathbf{s} = I$.

4.1 The Effect on Multipole Errors

For the effect on the multipole errors the radial field is needed and can be derived from the vector potential obtained from Eq. (19). Then the normal multipole errors are given by

$$B_{n,\text{Tube}} = -\frac{\mu_1 I}{2\pi} \frac{r_0^{n-1}}{r_I^n} \left(1 - \alpha_{12} \frac{\left(\frac{r_I}{a}\right)^{2n} - \left(\frac{r_I}{b}\right)^{2n}}{1 - \alpha_{12}^2 \left(\frac{a}{b}\right)^{2n}} \right). \quad (23)$$

The difference to the multipole error calculated by means of the imaging method is given by:

$$\Delta B_{n,\text{Tube}} = B_{n,\text{Tube}} - B_{n,\text{Bore}} \quad (24)$$

$$= \alpha_{12} \frac{1 - \alpha_{12}^2}{1 - \alpha_{12}^2 \left(\frac{a}{b}\right)^{2n}} \left(\frac{r_I}{b}\right)^{2n}. \quad (25)$$

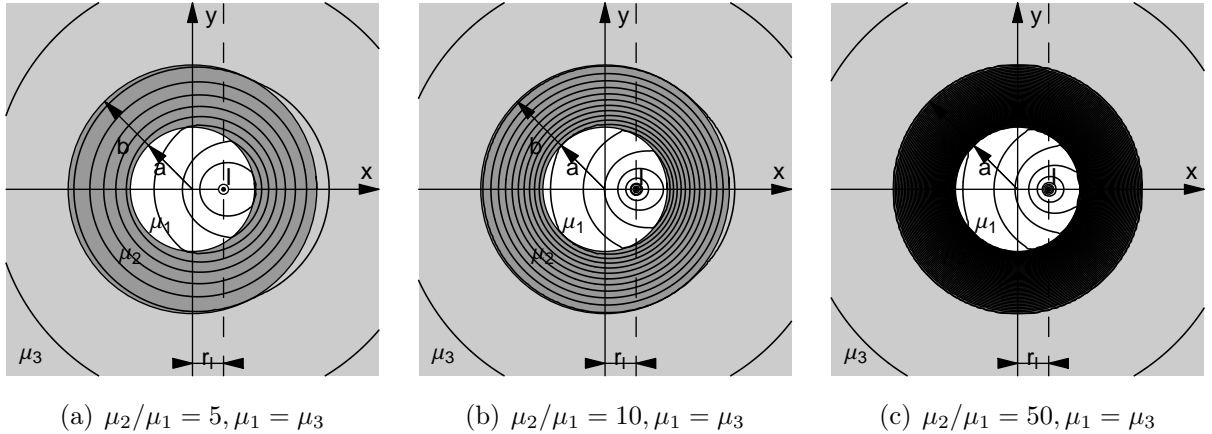


Figure 7: Field distribution of the magnetic induction for a line current inside a tube of permeable material.

For materials of high permeability the influence of the tube thickness reduces with increasing permeability since in this case α_{12} is close to -1 and for $a < b$ the fraction is smaller than 1. In this way the deviation is mainly driven by the fraction $(r_I/b)^n$ with $b \geq a > r_I$.

In fig. 8 the relative deviation $(\Delta B_{n,\text{Tube}}/B_{n,\text{Bore}})$ of the multipole errors for a tube with finite thickness compared to the multipole errors of a bore is shown. The positioning radius r_I is set to half of the inner tube radius. The dashed lines indicate a relative deviation of -0.1% and the continuous lines of -1% . It can be seen that for yokes of an outer radius of more than three times the inner radius the modulus of the deviation is smaller than 1% for all multipoles. Furthermore it can be seen that for high permeabilities and therefore values of α close to -1 the absolute deviation is much smaller even if the outer radii are only 1.5 times the inner radius. Generally the influence of the tube thickness is strongly depending on the order of the multipole error and for thick tubes it is only significant up to the order of 3.

In order to show how to use fig. 8 one example is given: Considering a yoke of outer radius 2.5 times the inner radius and an α of -0.8 this yields a deviation of little more than -1% for the main field (B_1) because it is inside and close to the continuous line indicated by 1 and an absolute deviation of less than 0.1% for all other multipoles since the point is outside all higher order dashed lines.

4.2 Fringe Field of a Coil

For the operation of superconducting magnets it is important to make sure that the field outside the magnet, the so-called fringe field, does not exceed certain limits. This stray field could cause problems with other electrical devices, cause movement of iron parts or even effect the health of persons exposed to it [7].

It is obvious that the strength of the fringe field increases with increasing main field and therefore it is most severe for a magnet operated at maximum field. As mentioned

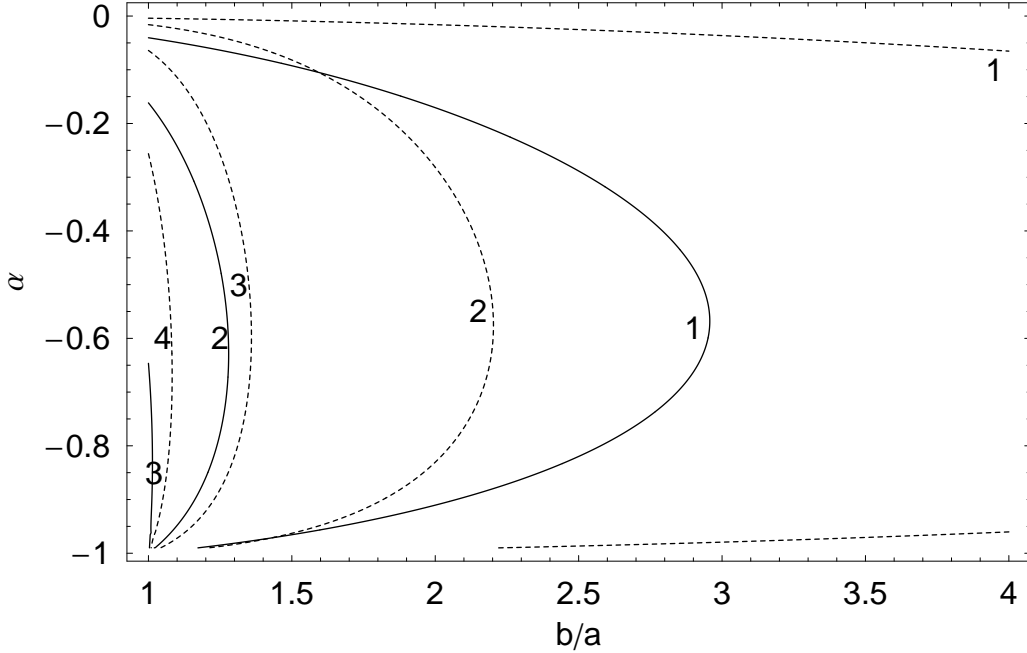


Figure 8: The relative deviation of the multipole errors for a tube of varying thickness and permeability compared to a bore of fixed inner radius. The positioning radius r_I is assumed to be half the inner tube radius a . The parameter α denotes the imaging coefficient as defined in Eq. (64). The continuous lines indicate a deviation of -1% compared to the calculation with the imaging method. The dashed lines indicate a deviation of -0.1% . The numbers denote the order of the multipole error.

above, for high fields the iron saturation has to be taken into account and a calculation has to be done by means of numerical field computation.

Nevertheless, an analytical expression shall be derived from the expressions obtained before to be used for first estimations and investigations. Therefore a coil of two leads is considered in order to represent the bipolar character of symmetric coils.

From Eq. (22), the vector potential and the field of magnetic induction of a coil can be derived in the area outside the tube.

$$A_{3,z} = \frac{\mu_1 I}{2\pi} \sum_{n=1}^{\infty} \frac{1}{n} \frac{\beta_{12}(1 - \alpha_{12})}{1 - \alpha_{12}^2 \left(\frac{a}{b}\right)^{2n}} \left(\frac{r_I}{\rho}\right)^n \cos(n\phi) [1 - \cos(n\pi)] \quad (26)$$

$$B_{3,\rho} = -\frac{\mu_1 I}{2\pi} \sum_{n=1}^{\infty} \frac{\beta_{12}(1 - \alpha_{12})}{1 - \alpha_{12}^2 \left(\frac{a}{b}\right)^{2n}} \frac{r_I^n}{\rho^{n+1}} [1 - \cos(n\pi)] \sin(n\phi) \quad (27)$$

$$B_{3,\phi} = \frac{\mu_1 I}{2\pi} \sum_{n=1}^{\infty} \frac{\beta_{12}(1 - \alpha_{12})}{1 - \alpha_{12}^2 \left(\frac{a}{b}\right)^{2n}} \frac{r_I^n}{\rho^{n+1}} [1 - \cos(n\pi)] \cos(n\phi) \quad (28)$$

Figure 9 shows the field distribution of a symmetric coil of two leads in an iron tube with a relative permeability of 10. For the LHC main dipoles, this permeability value would be

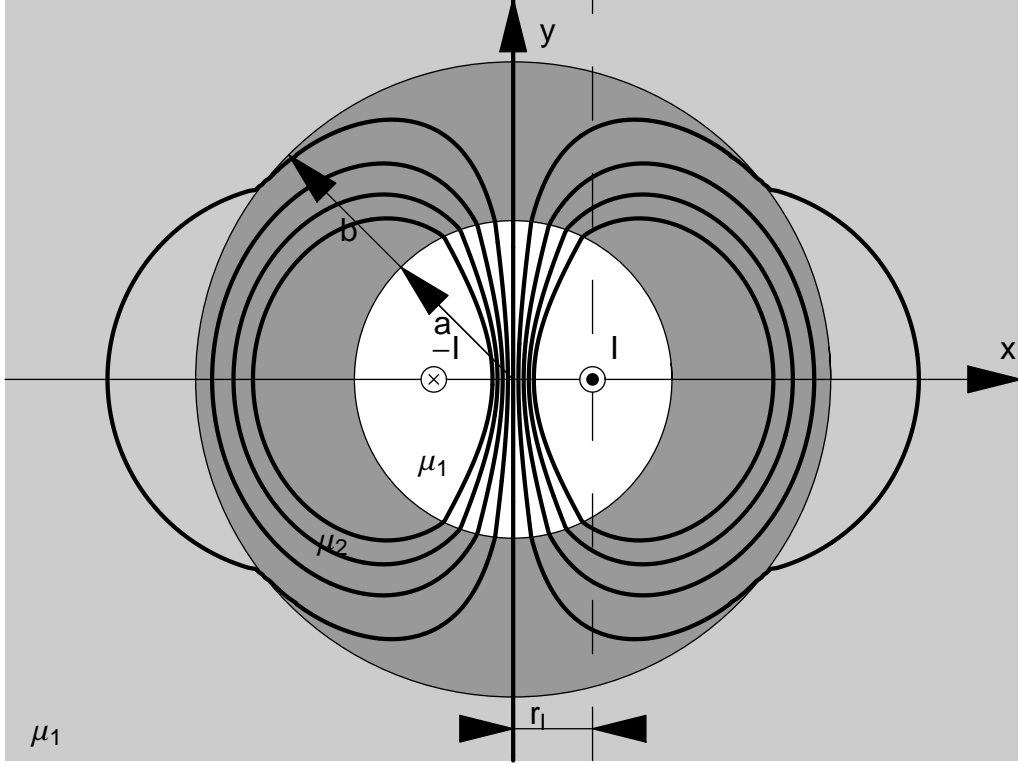


Figure 9: Field distribution of the magnetic induction for a coil in a permeable tube. The positioning radius is half the inner yoke radius. The outer yoke radius is twice the inner yoke radius and the permeability of the tube is 10 times bigger then the permeability of the air domain.

below saturation of the yoke. The resulting fringe field is easily observable.

The modulus of a vector field in cylindrical coordinates can be calculated by the square root of the square sum of the components of the vector, $|\mathbf{B}| = \sqrt{B_\rho^2 + B_\phi^2 + B_z^2}$. It is then possible to define the coefficients k_{nm} by

$$k_{nm}(\rho) = \beta_{12}^2 (1 - \alpha_{12})^2 \frac{(1 - \cos(n\pi))(1 - \cos(m\pi))}{\left(1 - \alpha_{12}^2 \left(\frac{a}{b}\right)^{2n}\right) \left(1 - \alpha_{12}^2 \left(\frac{a}{b}\right)^{2m}\right)} \frac{r_I^{2n}}{\rho^{n+m+2}} \quad (29)$$

which only differs from zero for odd m and n , and express the modulus by:

$$|\mathbf{B}| = \frac{\mu_1 |I|}{2\pi} \sqrt{\sum_{\substack{n=1 \\ m=1}}^{\infty} k_{nm} \cos((n-m)\phi)}. \quad (30)$$

In fig. 10 the maximum of the modulus of the fringe field is displayed for different outer yoke radii and permeabilities. The inner yoke radius is chosen to 125 mm which is similar

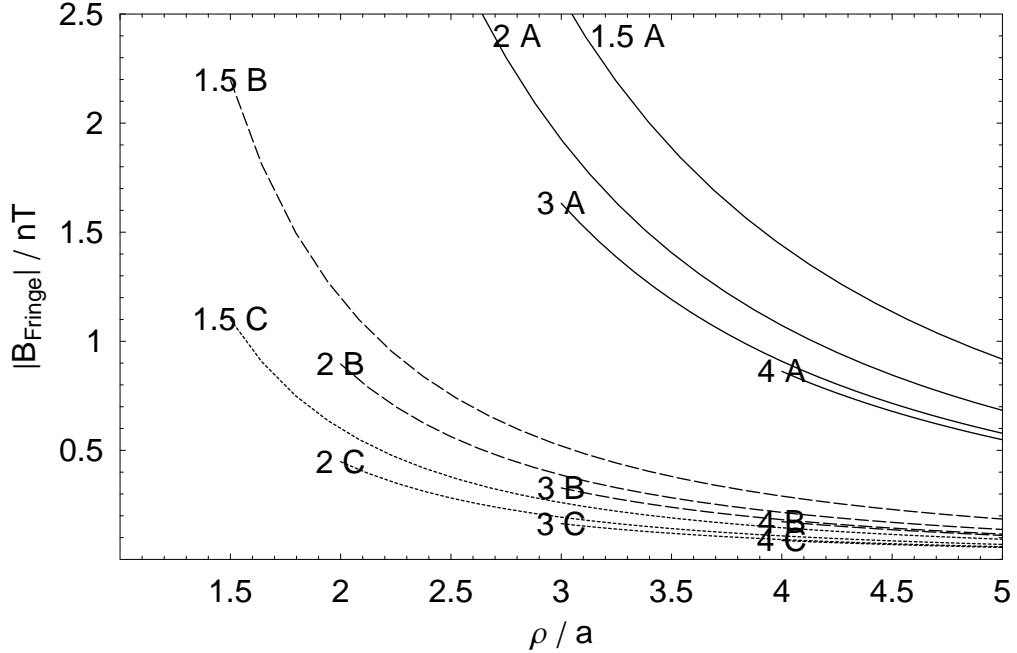


Figure 10: Modulus of the fringe field along the x -axis for different outer tube radii and tube permeabilities. The numbers indicate the outer tube radii in fractions of the inner tube radius. The capital letters indicate the used relative permeability of the tube material ($A = 500$, $B = 2500$ and $C = 5000$). The inner tube radius a is 125 mm, the current I is 1 A and the position of the currents r_I is $a/2$.

to the radius used for the study of the NED 88 mm aperture dipole. The line currents of ± 1 A are placed at $r_I = a/2$. Assuming a linear material the results can be scaled to any currents (or ampere turns).

It has to be emphasized that due to saturation effects at high fields the fringe field of real geometries will exceed the values given above. In this case, the formulae defines only the lower bounds.

In [8, p. 228] JACKSON calculates the screening of the magnetic field of a line current due to a surrounding permeable cylinder by using the scalar potential approximation of a line dipole of first order, and gives the screening factor F to

$$F = \frac{4\mu_r b^2}{(\mu_r + 1)^2 b^2 - (\mu_r - 1)^2 a^2}.$$

This equals the first coefficient ($n = 1$) of the vector potential given in Eq. (26) and confirms the expressions given.

5 The Influence of the Steel Collar

Superconducting coils are usually surrounded by rigid force-retaining structures in order to withstand the enormous electromagnetic forces and to provide prestress to the coil. The force-retaining structure typically consists of a combination of a collar made of stainless steel or aluminum and a surrounding iron yoke made of magnetic steel. This method increases the minimum distance between the iron yoke and the coil, however, the collar represents a second material which has to be modeled independently.

A first estimation of the influence of the collar on the multipole errors can be derived by modeling a circular collar (neglecting, *e.g.*, notches and noses along the inner contour of the collars) by means of the general solution of the three material problem derived in appendix B. From Eq. (1), the radial magnetic field and the normal multipole errors can be calculated. Here, the entity μ_1 denotes the permeability in the region of the bore and μ_2 is the material permeability of the collars, used to determine α_{12} .

$$B_{n,\text{Collar}} = -\frac{\mu_1 I r_0^{n-1}}{2\pi r_I^n} \left(1 - \frac{\alpha_{12} \left(\frac{r_I}{a}\right)^{2n} + \alpha_{23} \left(\frac{r_I}{b}\right)^{2n}}{1 + \alpha_{12}\alpha_{23} \left(\frac{a}{b}\right)^{2n}} \right) \quad (31)$$

Figure 11 shows the relative deviation of the multipole errors if calculated with and without collars made of a material with low permeability. The mean positioning radius r_I of the coil is set to 0.075 m and the inner collar radius a is set to 0.1 m. The inner yoke radius b is given by the varied collar thickness d to $b = a + d$. The relative permeability of the iron yoke is set to 500 while the permeability of the collar is also varied. It can be seen that the influence of the collar material on the multipole errors decreases strongly with increasing multipole order. For materials with a relative permeability below 2 the contribution of the collar is very small and translates to a change of relative multipoles of approximately 1%.

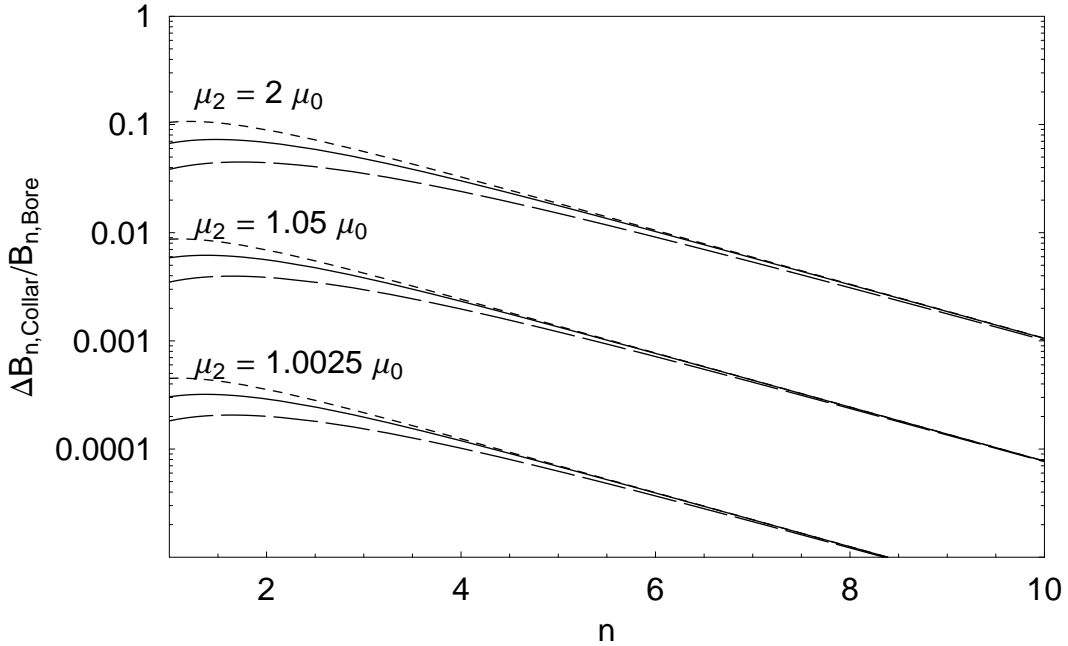


Figure 11: Influence of the collar on the multipole error. The continuous lines represent a geometry of inner collar radius a of 0.1 m and collar thickness d of 0.025 m. For the dotted lines the collar thickness is increased to $d = 0.05$ m while for the dashed lines the collar thickness is decreased to $d = 0.0125$ m.

6 Conclusions

A general solution for the magnetic field is given for the general geometry of an eccentric line current placed in a circular domain and surrounded by two materials of different permeabilities (Appendix B). The solution is used for the calculation of a single line current

- inside a *bore* in permeable material,
- inside a *tube* of permeable material, and
- inside a *tube of low permeability* surrounded by material of higher permeability.

In magnet applications, the results allow to decide whether the contribution of the iron yoke can be determined analytically or whether a collar of stainless steel has to be considered in the calculation. Therefore, the so-called imaging method for a single line current in a circular bore was derived and it could be demonstrated that

- the boundary conditions for a single line current in a bore within material with infinitely permeability can be fulfilled without violating AMPERE's law, and
- that the closing lead, usually not considered for the calculation of a single line current, has to be taken into account when the imaging method is applied.

Using the imaging method,

- the influence of the iron yoke on the multipole errors can be shown, and
- the limit of the model due to the iron saturation is estimated.

For the latter two geometries it is shown,

- that for the radii and permeabilities commonly used for the iron yoke of superconducting magnets, the imaging method is sufficient to calculate the effect of the iron yoke on the multipole errors in the non saturated state,
- how to estimate the fringe field and how it decreases with increasing distance to the yoke, and
- that for the commonly used low permeabilities of the collar material, and the circular shape, the collar does not need to be considered within the analytical calculations. It should be noted that for the case of non-circular collar contours, the contribution of the collars should be determined differently.

The validity of the imaging method for the modeling of superconducting magnets has been shown and the limiting factors as the yoke thickness and the maximum allowed current, the saturation current, were pointed out.

7 Acknowledgments

The authors wish to thank E. Todesco, for his comments on the manuscript.

References

- [1] S. Russenschuck, *Electromagnetic Design and Optimization of Accelerator Magnets*, 1st ed. Geneva, Switzerland: CERN, Apr. 2005, ISBN: 92-9083-242-8.
- [2] S. Kawabata, “Magnetic permeability of the iron yoke in high field superconducting magnets,” *Nuclear Instruments and Methods in Physics Research*, vol. A, pp. 1–8, 1993.
- [3] G. Morgan, “Use of an elliptical aperture to control saturation in closely-coupled, cold iron, superconducting dipole magnets,” in *IEEE Transactions On Nuclear Science*, vol. NS-32, no. 5, BNL. Upton, New York, USA: IEEE, Oct. 1985, pp. 3695–3697.
- [4] N. Schwerg, “Electromagnetic Design Study for a Large Bore 15T Superconducting Dipole Magnet,” Diploma Thesis, Technische Universität Berlin, Berlin, Germany, Nov. 2005. [Online]. Available: <http://cdsweb.cern.ch/search.py?recid=914515&ln=en>
- [5] W. Ansorge, “Some basic design parameters of the isr sc quadrupole,” Internal Note ISR-MA/WA/rh, CERN, Geneva, Switzerland, Nov. 1973.
- [6] A. Devred and D. Trassart, “Magnetic Field Produced by a Single Current Line near or within a Ferromagnetic Cylinder or Tube,” Departmental Report, Geneva, Switzerland, July 2005. [Online]. Available: <http://doc.cern.ch/archive/electronic/cern/preprints/at/at-2005-010.pdf>
- [7] “Safety Rules for the Use of Static Magnetic Fields at CERN,” IS36 Rev. 2, Geneva, Switzerland, June 2005. [Online]. Available: https://edms.cern.ch/file/335801/3/IS36_E.pdf
- [8] J. D. Jackson, *Classical Electrodynamics*, 3rd ed. New York, USA: John Wiley and Sons, 1999.
- [9] H. Henke, *Elektromagnetische Felder*, 1st ed. Heidelberg, Germany: Springer, 2001.

A Field Quality and Multipole Expansion

The multipole field errors can be obtained from the FOURIER expansion of the radial magnetic induction, B_r , inside a magnet's aperture at a given reference radius, R_{ref} :

$$B_r(R_{\text{ref}}, \phi) \approx \sum_{n=1}^{N_m} [A_n(R_{\text{ref}}) \cos(n\phi) + B_n(R_{\text{ref}}) \sin(n\phi)] \quad (32)$$

where N_m denotes the highest order coefficient taken into account, A_n the skew and B_n the normal multipole errors given by:

$$A_n(R_{\text{ref}}) = \frac{1}{\pi} \int_0^{2\pi} B_r(R_{\text{ref}}, \phi) \cos(n\phi) d\phi \quad (33)$$

$$B_n(R_{\text{ref}}) = \frac{1}{\pi} \int_0^{2\pi} B_r(R_{\text{ref}}, \phi) \sin(n\phi) d\phi. \quad (34)$$

Dividing the multipole coefficients by the main component of the magnet configuration, B_N , and multiplying by 10^4 yields the so-called relative multipole errors, a_n and b_n :

$$a_n(R_{\text{ref}}) = \frac{A_n(R_{\text{ref}})}{B_N(R_{\text{ref}})} 10^4, \quad b_n(R_{\text{ref}}) = \frac{B_n(R_{\text{ref}})}{B_N(R_{\text{ref}})} 10^4. \quad (35)$$

B Magnetic Induction and Vector Potential for a Circular Problem consisting of 3 material layers

We consider a circular hollow cylinder with inner radius a and outer radius b . The circular bore, the cylinder and the outside shall have the material permeabilities μ_1 , μ_2 and μ_3 . Inside the hollow cylinder one straight line current I is placed at the arbitrary position $x = r_I$.

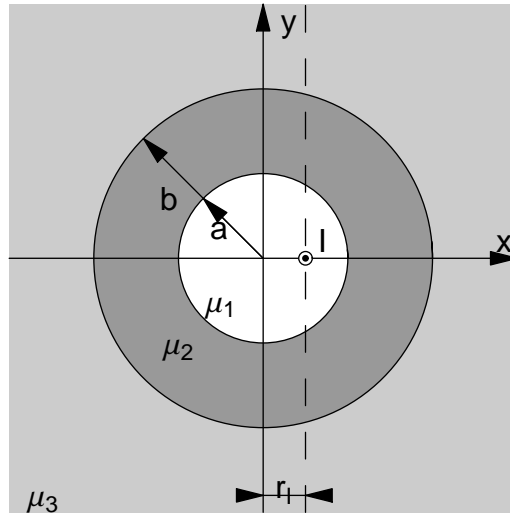


Figure 12: Geometry of a circular hollow cylinder of inner radius a and outer radius b . The tube shall have a material permeability μ_2 with two materials of different permeabilities μ_1 and μ_3 , inside and outside of the tube.

B.1 Potential Approach

The field distribution will be expressed by means of the vector potential \mathbf{A} . For area 1 inside the hollow cylinder the vector potential \mathbf{A}_1 consists of the primary potential of the line current \mathbf{A}_I and of the secondary potential $\mathbf{A}^{(1)}$ describing the repercussion of the iron on the inner field. In the areas 2 and 3 the field is created by the line current and the effect of the different materials and is expressed by the potentials $\mathbf{A}_2 = \mathbf{A}^{(2)}$ and $\mathbf{A}_3 = \mathbf{A}^{(3)}$.

$$\mathbf{A}_1 = \mathbf{A}_I + \mathbf{A}^{(1)}.$$

$\mathbf{A}^{(i)}$ with $n = 1, 2, 3$ denotes potential approaches for which the constants need to be determined in the following.

Since the source is a z -directed line current, all resulting vector potentials possess a z -component, only.

In [1] the vector potential of a single line current at an arbitrary radial position r_I is derived and expressed by means of the FOURIER expansion. In order to determine the

constants of the approaches the vector potential needs to be evaluated at the inner radius a , *i.e.* for radii bigger than the position of the line current. For the determination of multipole errors the potential is also needed for smaller radii.

$$\begin{aligned}
A_{|,z} &= -\frac{\mu_1 I}{2\pi} \ln \left(\frac{\sqrt{(x-r_I)^2 + y^2}}{R_0} \right) \\
&= -\frac{\mu_1 I}{2\pi} \begin{cases} \ln \left(\frac{r_I}{R_0} \right) - \sum_{n=1}^{\infty} \frac{1}{n} \left(\frac{\rho}{r_I} \right)^n \cos(n\phi) & \rho < r_I \\ \ln \left(\frac{\rho}{R_0} \right) - \sum_{n=1}^{\infty} \frac{1}{n} \left(\frac{r_I}{\rho} \right)^n \cos(n\phi) & \rho > r_I \end{cases}. \quad (36)
\end{aligned}$$

The secondary potentials can be expressed by the general solution of the LAPLACE-equation in cylindrical coordinates:

$$\begin{aligned}
A_z^{(i)} &= \frac{\mu_i I}{2\pi} \left(A_0^{(i)} + B_0^{(i)} \ln \left(\frac{\rho}{R_0} \right) \right) \left(C_0^{(i)} + D_0^{(i)} \phi \right) \\
&+ \frac{\mu_i I}{2\pi} \sum_{n=1}^{\infty} \frac{1}{n} \left(A_n^{(i)} \left(\frac{\rho}{r_I} \right)^n + B_n^{(i)} \left(\frac{r_I}{\rho} \right)^n \right) \left(C_n^{(i)} \cos(n\phi) + D_n^{(i)} \sin(n\phi) \right). \quad (37)
\end{aligned}$$

Before the constants of these approaches are determined by fulfilling the boundary conditions the number of unknowns can be reduced by qualitative thoughts:

One line current placed at an arbitrary position on the x -axis produces circular field lines which are always perpendicular to the x -axis. Although the field distribution is changed by the repercussion of the hollow cylinder, this characteristic will stay unchanged and so the field of the magnetic induction will be only azimuthal for $\phi = 0$ and $\phi = \pi$. For this reason all sine-terms and the linearly ϕ -dependent term vanish.

$$D_0^{(1,2,3)} = 0, \quad (38)$$

$$D_n^{(1,2,3)} = 0. \quad (39)$$

In area 1, the only singularity is at the position of the line current. Therefore, the value of the vector potential has to be finite.

$$B_0^{(1)} = 0, \quad (40)$$

$$B_n^{(1)} = 0. \quad (41)$$

For very big radii all fields should vanish and so the term with ρ^n has to vanish in area 3.

$$A_n^{(3)} = 0. \quad (42)$$

With these first constants the approaches can be reduced and the following constants can be defined:

$$\begin{aligned}
L_0^{(1)} &= A_0^{(1)} C_0^{(1)}, & E_n^{(1)} &= A_n^{(1)} C_n^{(1)}, \\
L_0^{(2)} &= A_0^{(2)} C_0^{(2)}, & K_0^{(2)} &= B_0^{(2)} C_0^{(2)}, & E_n^{(2)} &= A_n^{(2)} C_n^{(2)}, & F_n^{(2)} &= A_n^{(2)} C_n^{(2)}, \\
L_0^{(3)} &= A_0^{(3)} C_0^{(3)}, & K_0^{(3)} &= B_0^{(3)} C_0^{(3)}, & F_n^{(3)} &= B_n^{(3)} C_n^{(3)}.
\end{aligned}$$

Then the secondary vector potentials read:

$$A_z^{(1)} = \frac{\mu_1 I}{2\pi} \left[L_0^{(1)} + \sum_{n=1}^{\infty} \frac{1}{n} E_n^{(1)} \left(\frac{\rho}{r_I} \right)^n \cos(n\phi) \right], \quad (43)$$

$$A_z^{(2)} = \frac{\mu_2 I}{2\pi} \left[L_0^{(2)} + K_0^{(2)} \ln \left(\frac{\rho}{R_0} \right) + \sum_{n=1}^{\infty} \frac{1}{n} \left(E_n^{(2)} \left(\frac{\rho}{r_I} \right)^n + F_n^{(2)} \left(\frac{r_I}{\rho} \right)^n \right) \cos(n\phi) \right] \quad (44)$$

$$A_z^{(3)} = \frac{\mu_3 I}{2\pi} \left[L_0^{(3)} + K_0^{(3)} \ln \left(\frac{\rho}{R_0} \right) + \sum_{n=1}^{\infty} \frac{1}{n} F_n^{(3)} \left(\frac{r_I}{\rho} \right)^n \cos(n\phi) \right]. \quad (45)$$

B.2 Field of Magnetic Induction

The magnetic induction in the three areas is given by the curl of the vector potentials and yields:

$$B_{1,r}^{\rho < r_I} = -\frac{\mu_1 I}{2\pi} \sum_{n=1}^{\infty} (1 + E_n^{(1)}) \frac{\rho^{n-1}}{r_I^n} \sin(n\phi), \quad (46)$$

$$B_{1,\phi}^{\rho < r_I} = -\frac{\mu_1 I}{2\pi} \sum_{n=1}^{\infty} (1 + E_n^{(1)}) \frac{\rho^{n-1}}{r_I^n} \cos(n\phi), \quad (47)$$

$$B_{1,r}^{\rho > r_I} = -\frac{\mu_1 I}{2\pi} \sum_{n=1}^{\infty} \left(\frac{r_I^n}{\rho^{n+1}} + E_n^{(1)} \frac{\rho^{n-1}}{r_I^n} \right) \sin(n\phi), \quad (48)$$

$$B_{1,\phi}^{\rho > r_I} = \frac{\mu_1 I}{2\pi} \frac{1}{\rho} + \frac{\mu_1 I}{2\pi} \sum_{n=1}^{\infty} \left(\frac{r_I^n}{\rho^{n+1}} - E_n^{(1)} \frac{\rho^{n-1}}{r_I^n} \right) \cos(n\phi). \quad (49)$$

$$B_{2,r} = -\frac{\mu_2 I}{2\pi} \sum_{n=1}^{\infty} \left(E_n^{(2)} \frac{\rho^{n-1}}{r_I^n} + F_n^{(2)} \frac{r_I^n}{\rho^{n+1}} \right) \sin(n\phi), \quad (50)$$

$$B_{2,\phi} = -\frac{\mu_2 I}{2\pi} K_0^{(2)} \frac{1}{\rho} - \frac{\mu_2 I}{2\pi} \sum_{n=1}^{\infty} \left(E_n^{(2)} \frac{\rho^{n-1}}{r_I^n} - F_n^{(2)} \frac{r_I^n}{\rho^{n+1}} \right) \cos(n\phi). \quad (51)$$

$$B_{3,r} = -\frac{\mu_3 I}{2\pi} \sum_{n=1}^{\infty} F_n^{(3)} \frac{1}{\rho^{n+1}} \sin(n\phi), \quad (52)$$

$$B_{3,\phi} = -\frac{\mu_3 I}{2\pi} K_0^{(3)} \frac{1}{\rho} + \frac{\mu_3 I}{2\pi} \sum_{n=1}^{\infty} F_n^{(3)} \frac{r_I^n}{\rho^{n+1}} \cos(n\phi). \quad (53)$$

B.3 Fulfilling the Boundary Conditions

All fields have to fulfill the boundary condition of continuous normal magnetic induction due to the zero divergence. Following AMPERE's law the tangential magnetic field is also continuous, if there are no current sheets on the boundary.

For very long geometries of which the cross section can be considered only, the vector potential results to

$$\mathbf{B}_1|_{\partial_{12}} \cdot \mathbf{n} = \mathbf{B}_2|_{\partial_{12}} \cdot \mathbf{n} \rightarrow A_1|_{\partial_{12}} = A_2|_{\partial_{12}}, \quad (54)$$

$$\mathbf{H}_1|_{\partial_{12}} \times \mathbf{n} = \mathbf{H}_2|_{\partial_{12}} \times \mathbf{n} \rightarrow \frac{1}{\mu_1} \frac{\partial \mathbf{A}_1}{\partial n} \Big|_{\partial_{12}} = \frac{1}{\mu_2} \frac{\partial \mathbf{A}_2}{\partial n} \Big|_{\partial_{12}}. \quad (55)$$

Here ∂_{12} denotes the boundary between areas 1 and 2, \mathbf{n} denotes a normal vector perpendicular to the boundary and $\partial/\partial n$ denotes its normal derivative ($\mathbf{n} \cdot \nabla$).

The considered geometry has one circular boundary at $\rho = a$ and one at $\rho = b$. This yields in general four equations. Furthermore, on the boundary the two vector potentials/ magnetic fields are the FOURIER expansion of the same function/quantity and thus show the same coefficients. The four equations can therefore be split up in one set for the members of each series of order zero and one set for the members of each series of n^{th} order.

The boundary condition $A_{z,1}|_{\rho=a} = A_{z,2}|_{\rho=a}$ yields:

$$L_0^{(1)} - \ln\left(\frac{a}{R_0}\right) = \frac{\mu_2}{\mu_1} \left(L_0^{(2)} + K_0^{(2)} \ln\left(\frac{a}{R_0}\right) \right), \quad (56)$$

$$\left(\frac{r_I}{a}\right)^n + E_n^{(1)} \left(\frac{a}{r_I}\right)^n = \frac{\mu_2}{\mu_1} \left(E_n^{(2)} \left(\frac{a}{r_I}\right)^n + F_n^{(2)} \left(\frac{r_I}{a}\right)^n \right). \quad (57)$$

The boundary condition $-\frac{1}{\mu_1} \frac{\partial A_{z,1}}{\partial \rho} \Big|_{\rho=a} = -\frac{1}{\mu_2} \frac{\partial A_{z,2}}{\partial \rho} \Big|_{\rho=a}$ yields:

$$\frac{1}{a} = -K_0^{(2)} \frac{1}{a}, \quad (58)$$

$$-E_n^{(1)} \frac{a^{n-1}}{r_I^n} + \frac{r_I^n}{a^{n+1}} = -E_n^{(2)} \frac{a^{n-1}}{r_I^n} + F_n^{(2)} \frac{r_I^n}{a^{n+1}}. \quad (59)$$

The boundary condition $A_{z,2}|_{\rho=b} = A_{z,3}|_{\rho=b}$ yields:

$$\frac{\mu_2}{\mu_3} \left(L_0^{(2)} + K_0^{(2)} \ln\left(\frac{b}{R_0}\right) \right) = L_0^{(3)} + K_0^{(3)} \ln\left(\frac{b}{R_0}\right), \quad (60)$$

$$\frac{\mu_2}{\mu_3} \left(E_n^{(2)} \left(\frac{b}{r_I}\right)^n + F_n^{(2)} \left(\frac{r_I}{b}\right)^n \right) = F_n^{(3)} \left(\frac{r_I}{b}\right)^n. \quad (61)$$

The boundary condition $-\frac{1}{\mu_2} \frac{\partial A_{z,2}}{\partial \rho} \Big|_{\rho=b} = -\frac{1}{\mu_3} \frac{\partial A_{z,3}}{\partial \rho} \Big|_{\rho=b}$ yields:

$$-K_0^{(2)} \frac{1}{b} = -K_0^{(3)} \frac{1}{b}, \quad (62)$$

$$-E_n^{(2)} \frac{b^{n-1}}{r_I^n} + F_n^{(2)} \frac{r_I^n}{b^{n+1}} = F_n^{(3)} \frac{r_I^n}{b^{n+1}}. \quad (63)$$

The two systems, one consisting of the four equations (56), (58), (60) and (62), the other consisting of the four equations (57), (59), (61) and (63), are solved by GAUSS' method or

by inversion of the matrix of the linear system. The system of the members of zero order is over determined which means that one of the three constants $L_0^{(1,2,3)}$ is free of choice. Without limitations the constant $L_0^{(3)}$ is set to zero.

In order to simplify the results and for coherence with literature [9] the constants α_{nm} and β_{nm} are defined for each boundary. Figure 13 shows the plot of both constants for different values for the corresponding permeability ratios between two areas

$$\alpha_{nm} = \frac{\mu_n - \mu_m}{\mu_n + \mu_m}, \quad (64)$$

$$\beta_{nm} = \frac{2\mu_n}{\mu_n + \mu_m}. \quad (65)$$

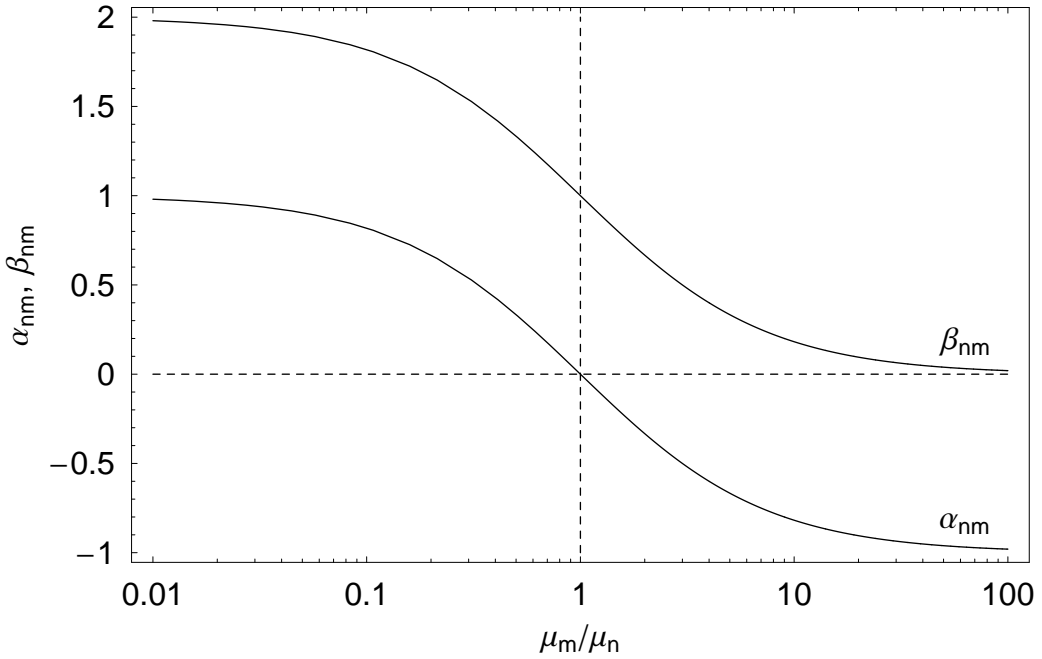


Figure 13: Values of the constants α_{nm} and β_{nm} for different permeabilities. The relation, $\beta_{nm} = \alpha_{nm} + 1$, can easily be observed.

This way the solution for the unknown constants reads:

$$L_0^{(1)} = \frac{\mu_1 - \mu_2}{\mu_1} \ln \left(\frac{a}{R_0} \right) + \frac{\mu_2 - \mu_3}{\mu_1} \ln \left(\frac{b}{R_0} \right), \quad (66)$$

$$K_0^{(2)} = -1, \quad L_0^{(2)} = \frac{\mu_2 - \mu_3}{\mu_2} \ln \left(\frac{b}{R_0} \right), \quad (67)$$

$$K_0^{(3)} = -1, \quad L_0^{(3)} = 0, \quad (68)$$

$$E_n^{(1)} = -\frac{\alpha_{12} \left(\frac{r_I}{a}\right)^{2n} + \alpha_{23} \left(\frac{r_I}{b}\right)^{2n}}{1 + \alpha_{12}\alpha_{23} \left(\frac{a}{b}\right)^{2n}}, \quad (69)$$

$$E_n^{(2)} = -\frac{\alpha_{23}\beta_{12} \left(\frac{r_I}{b}\right)^{2n}}{1 + \alpha_{12}\alpha_{23} \left(\frac{a}{b}\right)^{2n}}, \quad F_n^{(2)} = \frac{\beta_{12}}{1 + \alpha_{12}\alpha_{23} \left(\frac{a}{b}\right)^{2n}}, \quad (70)$$

$$F_n^{(3)} = \frac{\beta_{12}\beta_{23}}{1 + \alpha_{12}\alpha_{23} \left(\frac{a}{b}\right)^{2n}}. \quad (71)$$

B.4 The Resulting Vector Potential

With the constants derived above the vector potential is given for all three areas:

$$A_{1,z}^{\rho < r_I} = \frac{(\mu_1 - \mu_2)I}{2\pi} \ln\left(\frac{a}{R_0}\right) + \frac{(\mu_2 - \mu_3)I}{2\pi} \ln\left(\frac{b}{R_0}\right) - \frac{\mu_1 I}{2\pi} \ln\left(\frac{r_I}{R_0}\right) \\ + \frac{\mu_1 I}{2\pi} \sum_{n=1}^{\infty} \frac{1}{n} \left(\left(\frac{\rho}{r_I}\right)^n - \frac{\alpha_{12} \left(\frac{\rho}{a^2/r_I}\right)^n + \alpha_{23} \left(\frac{\rho}{b^2/r_I}\right)^n}{1 + \alpha_{12}\alpha_{23} \left(\frac{a}{b}\right)^{2n}} \right) \cos(n\phi), \quad (72)$$

$$A_{1,z}^{\rho > r_I} = \frac{(\mu_1 - \mu_2)I}{2\pi} \ln\left(\frac{a}{R_0}\right) + \frac{(\mu_2 - \mu_3)I}{2\pi} \ln\left(\frac{b}{R_0}\right) - \frac{\mu_1 I}{2\pi} \ln\left(\frac{\rho}{R_0}\right) \\ + \frac{\mu_1 I}{2\pi} \sum_{n=1}^{\infty} \frac{1}{n} \left(\left(\frac{r_I}{\rho}\right)^n - \frac{\alpha_{12} \left(\frac{\rho}{a^2/r_I}\right)^n + \alpha_{23} \left(\frac{\rho}{b^2/r_I}\right)^n}{1 + \alpha_{12}\alpha_{23} \left(\frac{a}{b}\right)^{2n}} \right) \cos(n\phi), \quad (73)$$

$$A_{2,z} = \frac{(\mu_2 - \mu_3)I}{2\pi} \ln\left(\frac{b}{R_0}\right) - \frac{\mu_2 I}{2\pi} \ln\left(\frac{\rho}{R_0}\right) \\ + \frac{\mu_2 I}{2\pi} \sum_{n=1}^{\infty} \frac{1}{n} \frac{-\alpha_{23}\beta_{12} \left(\frac{\rho}{b^2/r_I}\right)^n + \beta_{12} \left(\frac{r_I}{\rho}\right)^n}{1 + \alpha_{12}\alpha_{23} \left(\frac{a}{b}\right)^{2n}} \cos(n\phi), \\ A_{3,z} = -\frac{\mu_3 I}{2\pi} \ln\left(\frac{\rho}{R_0}\right) \\ + \frac{\mu_3 I}{2\pi} \sum_{n=1}^{\infty} \frac{1}{n} \frac{\beta_{12}\beta_{23} \left(\frac{r_I}{\rho}\right)^n}{1 + \alpha_{12}\alpha_{23} \left(\frac{a}{b}\right)^{2n}} \cos(n\phi). \quad (74)$$

These results can easily be generalized to geometries with a single line current at any position (r_I, ϕ_I) in area 1 by rotating the coordinate system. Mathematically this is given by the substitution

$$\phi \rightarrow \phi - \phi_I.$$

C Permeable Bore

C.1 The Imaging Method for a Single Line Current

Investigating equations (9) to (12) in terms of the vector potential of a single line current $A_{|,z}(x, y)$, Eq. (36), like the primary potential and using the relation $1 = \beta_{nm} - \alpha_{nm}$ yields

$$A_{\text{Bore},1,z}(x, y) = L_0^{(1)} + A_{|,z}(x - r_I, y) - \alpha_{12}A_{|,z}(x - a^2/r_I, y), \quad (75)$$

$$A_{\text{Bore},2,3,z}(x, y) = \beta_{12}A_{|,z}(x - r_I, y) + \alpha_{12}A_{|,z}(x, y). \quad (76)$$

The expressions for the vector potential include the permeability constant of the corresponding area.

The vector potential within the bore is then given by the primary potential and the potential of a virtual image current at the distance a^2/r_I as given by the imaging method.

In the result for the vector potential outside the bore, the α term can be interpreted as the imaging current of the closing lead in infinite distance. By means of the imaging method this would be placed in the center.

This means that all plain geometries are *a priori* of zero current and charge sum and the parts not considered and placed somewhere very far away have to be taken into account for imaging purposes.

For a continuous vector potential the constant $L_0^{(1)}$ is needed. However, for the magnetic field and the field of magnetic induction it is of no meaning and therefore does not need to be taken into account for the physical interpretation of the equations above.

In fig. 3 a) to c) the field distribution of one single line current is shown for three different outer permeabilities. It can be seen from the plots that the more the outer permeability outranges the inner, the more the field density outside increases compared to inside. Seen from the outer area, this feature results from the fact, that the virtual line current that is placed in the center is weighted with the factor $\mu_2\alpha_{12}$. Consequently, for large values of μ_2 , *i.e.* if $\mu_2 \rightarrow \infty$, this product produces a large field contribution. At the same time the field density inside the bore increases only slightly. Note that this effect occurs only if the current sum inside the bore is different from zero. Otherwise, the centered line currents cancel out.

C.2 Material with Infinite Permeability

In a first glance it might seem impossible to put a single line current into a bore within material with infinite material because either AMPERE's law or the boundary conditions of orthogonal field lines would be violated.

Following HENKE [9, p. 163], the boundary conditions for a geometry free of current sheets can also be written as

$$\frac{\tan \theta_1}{\tan \theta_2} = \frac{H_{t1}/H_{n1}}{H_{t2}/H_{n2}} = \frac{\mu_1}{\mu_2}. \quad (77)$$

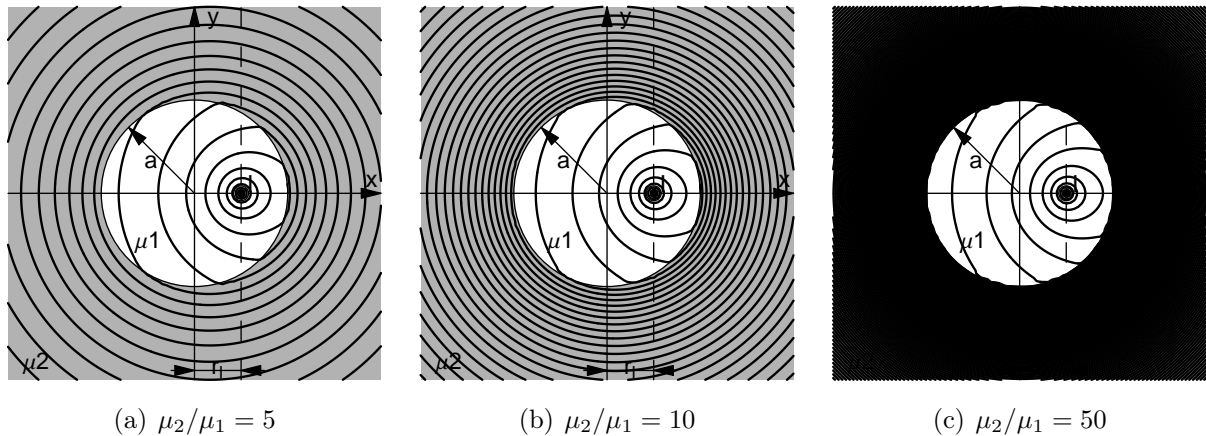


Figure 14: Field distribution of the magnetic induction for a line current inside a bore within permeable material. With increasing value of μ_2 the field density in area 2 increases, too.

Here H_{ti} denotes the tangential and H_{ni} denotes the normal component of the magnetic field on the boundary of area i . The angles θ_i denote the angle between the field/field lines and the normal vector on the boundary. The definition of the angles is also shown in fig. 15.

With an outer area of infinite permeability, the quotient of the two tangents is given to zero. This could be either obtained by an inner angle θ_1 of zero which means that the inner field lines run *perpendicular* to the boundary, or by an outer angle θ_2 of $\pi/2$ which means that field lines outside run *parallel* to the boundary of the bore.

From Eqs. (10) and (11) the magnetic field can be derived.

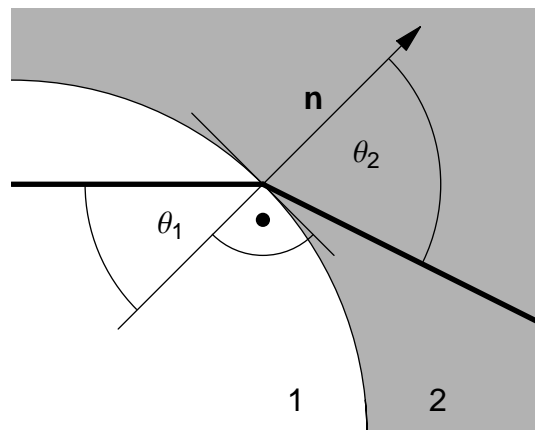


Figure 15: Definition of the angles of the field lines by means of a normal vector \mathbf{n} perpendicular to the contour. The two areas 1 and 2 are shown in different colors.

$$H_{1,\rho}^{\rho > r_I} = -\frac{I}{2\pi} \sum_{n=1}^{\infty} \left(\frac{r_I^n}{\rho^{n+1}} - \alpha_{12} \frac{\rho^{n-1}}{(a^2/r_I)^n} \right) \sin(n\phi), \quad (78)$$

$$H_{1,\phi}^{\rho > r_I} = \frac{I}{2\pi} \frac{1}{\rho} + \frac{\mu_1 I}{2\pi} \sum_{n=1}^{\infty} \left(\frac{r_I^n}{\rho^{n+1}} + \alpha_{12} \frac{\rho^{n-1}}{(a^2/r_I)^n} \right) \cos(n\phi), \quad (79)$$

$$H_{2,\rho}^{\rho > r_I} = -\beta_{12} \frac{I}{2\pi} \sum_{n=1}^{\infty} \frac{r_I^n}{\rho^{n+1}} \sin(n\phi), \quad (80)$$

$$H_{2,\phi}^{\rho > r_I} = \frac{I}{2\pi} \frac{1}{\rho} + \beta_{12} \frac{\mu_2 I}{2\pi} \sum_{n=1}^{\infty} \frac{r_I^n}{\rho^{n+1}} \cos(n\phi). \quad (81)$$

Calculating the arc tangent of the field components at $\rho = a$ and evaluating the limit for $\mu_2 \rightarrow \infty$ yields the two angles $\theta_{1,2}$:

$$\begin{aligned} \theta_1(\phi) &= \arctan \left(\frac{H_{1,\phi}(\rho = a)}{H_{1,\rho}(\rho = a)} \right) \\ &= \arctan \left(\frac{1}{-2 \sum_{n=1}^{\infty} \left(\frac{r_I}{a} \right)^n \sin(n\phi)} \right) \end{aligned} \quad (82)$$

$$\begin{aligned} \theta_2(\phi) &= \arctan \left(\frac{H_{2,\phi}(\rho = a)}{H_{2,\rho}(\rho = a)} \right) \\ &= \arctan \left(\frac{1}{\beta_{12} \rightarrow 0} \right) = \frac{\pi}{2} \end{aligned} \quad (83)$$

As shown in Eqs. (82) and (83), for a single line current in a permeable bore with $\mu \rightarrow \infty$ the latter case is applicable and the field lines are not perpendicular. Fig. 16 shows the angle of the field lines at the inner circular boundary of the bore.

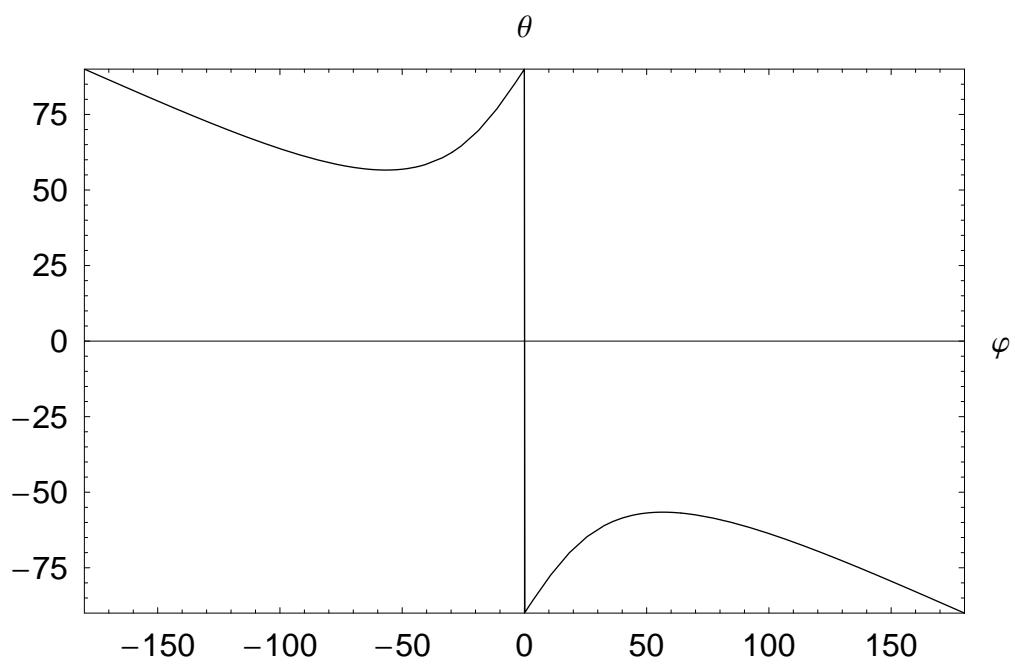


Figure 16: Angle of the field lines at the inner boundary of the circular bore within material with infinite permeability.